# Acoustic waves generated from seismic surface waves: propagation properties determined from Doppler sounding observations and normal-mode modelling

Juliette Artru, Thomas Farges, Philippe Lognonné

**HAL Id: insu-03600278**

**https://insu.hal.science/insu-03600278**

Submitted on 7 Mar 2022

# Acoustic waves generated from seismic surface waves: propagation properties determined from Doppler sounding observations and normal-mode modelling

Juliette Artru,[1] Thomas Farges[2] and Philippe Lognonné[3]

[1] *California Institute of Technology, Seismological Laboratory, Pasadena, California* 91107, *USA*
[2] *Commissariat à l'Énergie Atomique, Département Analyse Surveillance Environnement,* BP 12, 91680 *Bruyères-le Châtel, France*
[3] *Institut de Physique du Globe de Paris, Département de Géophysique Spatiale et Planétaire,* UMR7096, 4 *avenue de Neptune,* 94107
*Saint-Maur-des-Fossés, France*

**SUMMARY**

Since 1960, experiments have shown that perturbations of the ionosphere can occur after earthquakes, by way of dynamic coupling between seismic surface waves and the atmosphere. The atmospheric wave is amplified exponentially while propagating upwards due to the decrease of density, and interaction with the ionospheric plasma leads to clearly identified signals on both ground-based or satellite ionospheric measurements. In 1999 and 2000, after an upgrade of the HF Doppler sounder, the Commisariat à l'Énergie Atomique systematically recorded these effects in the ionosphere with the Francourville (France) network, by measuring vertical oscillations of ionospheric layers with the Doppler technique. Normal-mode theory extended to a solid Earth with an atmosphere allows successful modelling of such signals, even if this 1-D approach is probably too crude, especially in the solid Earth, where 20 s surface waves see large lateral variations in the crust. The combination of observations and simulations provides a new tool to determine acoustic gravity wave propagation characteristics from the ground to ionospheric height. Observed velocity and amplification of the atmospheric waves show good agreement from the ground up to moderate sounding altitudes (140–150 km); however, at higher altitudes the propagation speed is found to be much smaller than predicted and attenuation is underestimated. This shows that the standard formalism of acoustic gravity waves in the atmosphere cannot efficiently describe propagation in the ionized atmosphere. Further work is needed to characterize the propagation of acoustic waves in this altitude range: we believe that seismic waves can provide a well-constrained source for such study.

**Key words:** acoustic gravity waves, atmosphere, Doppler sounding, ionosphere, normal modes, surface waves.

## 1 INTRODUCTION

Solid Earth events such as earthquakes, volcanoes and tsunamis can generate atmospheric and ionospheric perturbations by various coupling mechanisms. Our focus here is on dynamic coupling: small vertical oscillations of the Earth's surface launch pressure waves in the neutral atmosphere that grow in amplitude by several orders of magnitude as they attain ionospheric heights. In particular, surface Rayleigh waves emanating from an earthquake cause ground displacements that can produce upwardly propagating acoustic waves.

The Doppler sounding technique allows continuous monitoring of the vertical displacement of a given ionospheric layer. From 1999 August to 2000 December, the network of Francourville (France),

after a major digital upgrade to a formerly analogue device, recorded most of the seismic signals from earthquakes of $M_w$ 6.5 or larger worldwide.

The interest of our study lies in the fact that, unlike most types of acoustic gravity waves, Rayleigh waves are very well constrained. It is possible to take advantage of the high precision of seismographic networks, seismic source determinations, and seismic wave modelling techniques, and from there to focus on the propagation of the perturbation in the atmosphere only. After a brief recall of the coupling mechanism and previous observations of these signals, we will present the observations used in the present study, as well as the technique developed to model such signals. We will then show what information about atmospheric structure we can infer from a joint study of the coupling.

## 2 SEISMIC ACOUSTIC WAVES

### 2.1 First observations

Ionospheric perturbations that follow earthquakes have been observed both near the seismic source and at teleseismic distances. The first published observations were obtained after the great Alaska earthquake in 1964. Using ionospheric sounding networks, Bolt (1964) and Davies & Baker (1965) observed perturbations showing both an atmospheric perturbation propagating from the epicentre region and the ionospheric signature of the Rayleigh wave propagation at the sounder location. An extensive literature exists that documents examples of the coupling between terrestrial events and the ionosphere. A review of earlier observations is found in Blanc (1985).

Recent works have similarly identified these two different types of coupling: Calais & Minster (1995) detected perturbations in the ionospheric total electron content above Southern California after the Northridge earthquake ($M_w = 6.7$, 1994 January 17) using GPS measurements; and Ducic *et al.* (2003) observed the perturbation associated with the Rayleigh wave propagation from the $M_w$ 7.9 Denali earthquake (2002 November 3) using a similar technique and were able to measure the horizontal group velocity of the waves in the ionosphere. Detection using satellite to ground receiver signals (GPS in these cases) is, however, challenging because it is sensitive to perturbations at high altitude, where most of the signal is already dissipated; furthermore, the integrated nature of the measurement acts as a low-pass first-order filter, and the TEC perturbations are not a direct measurement of the velocity field. As Doppler sounding networks can monitor oscillations of the lower ionospheric layers, they can usually detect most $M > 6.5$ earthquakes on a systematic

basis (Yuen *et al.* 1969; Blanc & Mercandalli-Rascalou 1992; Artru *et al.* 2001). Fig. 1 presents an example of such measurements after the 1999 November 12 Turkey earthquake, with a corresponding seismogram.

### 2.2 Atmospheric waves

The interaction of compression and gravitational forces gives rise to acoustic gravity waves in the atmosphere. The basic physics of acoustic gravity waves has been developed by Hines (1960), and we will review here its main features for a simple isothermal atmosphere in a hydrostatic model. The equations of motion in this model assume adiabatic motion and explicitly include as forces only inertia, gravity, and pressure gradients:

$$\text{Continuity} \quad : \frac{\partial \rho}{\partial t} + \mathbf{v} \cdot \nabla \rho = -\rho \nabla \cdot \mathbf{v},$$

$$\text{Momentum} \quad : \frac{\partial \mathbf{v}}{\partial t} + \mathbf{v} \cdot \nabla \mathbf{v} = \mathbf{g} - \frac{1}{\rho} \nabla p, \quad (1)$$

$$\text{Adiabaticity} \quad : \frac{\partial p}{\partial t} + \mathbf{v} \cdot \nabla p = C_s^2 \left( \frac{\partial \rho}{\partial t} + \mathbf{v} \cdot \nabla p \right),$$

where $\rho$ is the density, $p$ is the pressure, $\mathbf{v}$ is the neutral gas velocity, $\mathbf{g}$ is the acceleration due to gravity and $C_s$ is the constant sound speed. In the equilibrium state, $\mathbf{v}_0 = 0$ and both $\rho_0$ and $p_0$ are proportional to $\exp(z/2H)$, where $H = C_s^2/\gamma \mathbf{g}$ is the density scaleheight, $\gamma$ being the specific heat ratio. Assuming $\rho_1$, $p_1$, and $\mathbf{v}$ are small perturbations with no dependence along the *y*-axis, we can solve the linearized equations to obtain harmonic solutions with $\rho_1/\rho_0$, $p_1/p_0$ and $\mathbf{v}$ proportional to $\exp[i(\omega t - k_x x - k_z z)]$. If we define $k'_z = k_z + i/2H$, the following dispersion relation can be derived:
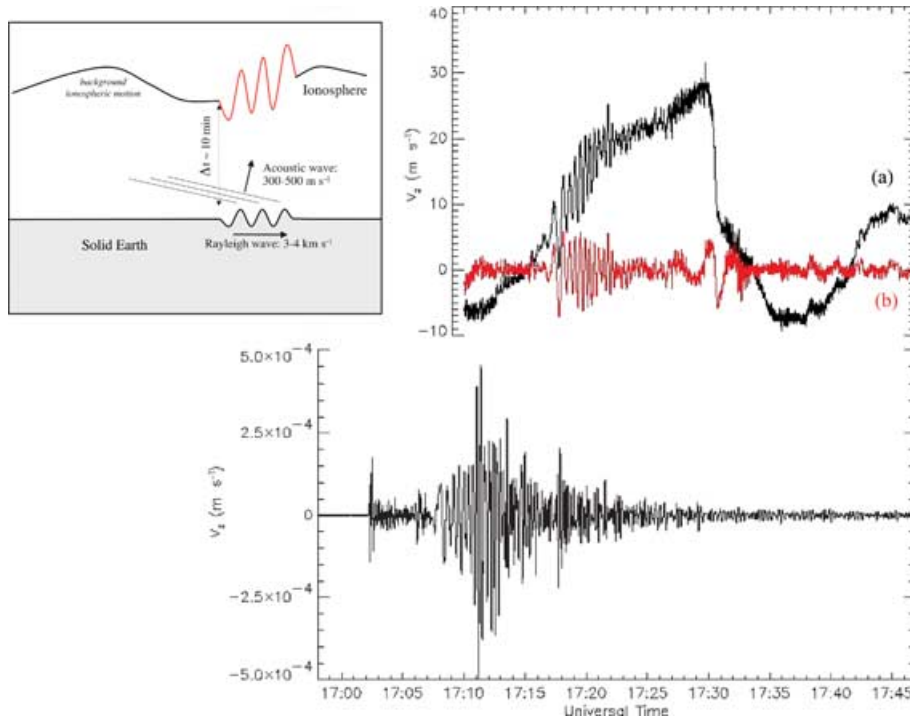


**Figure 1.** Comparison of the vertical velocity at ground level (bottom) measured at Lormes (France) and in the ionosphere at 221 km height (top) measured on the Francourville network just after the Turkey earthquake of 1999 November 12. The top black trace (a) is the unfiltered ionospheric signal, where some long-period variations unrelated to the earthquake appear. Trace (b) shows the same data filtered with a high-pass filter at 3.3 mHz (5 min). The delay of $\approx$10 min in the arrival time of the seismic signal corresponds to the propagation of the acoustic wave from the ground to 221 km. Left-hand panel shows the geometry of the coupled waves.
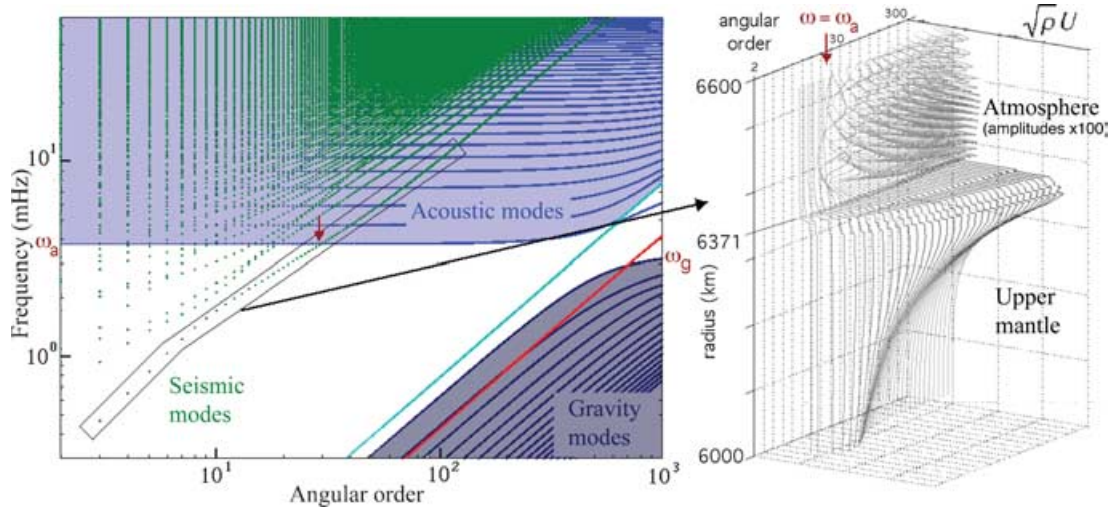
**Figure 2.** (Left panel) Domains of existence of acoustic and gravity waves as a function of frequency and angular order. Green dots are the discrete spectrum of solid Earth free spheroidal modes. Seismic waves couple with upward-propagating acoustic waves for frequencies higher than the acoustic cut-off frequency, here $\omega_a = 3.68$ mHz. (Right panel) Spheroidal solid normal modes are used for the summation. This figure represents energy ($\sqrt{\rho}U$, where $\rho$ is the density and $U$ the vertical displacement) for fundamental solid spheroidal modes with angular orders $l = 2$ to 200, as a function of radius. Two regimes are found. When $\omega < \omega_a$, the atmospheric part of the mode is trapped and decreases exponentially with altitude. At higher frequencies, in contrast, the energy propagates upwards. Viscous attenuation appears above an altitude of 100 km (radius >6470 km).

$$\left(\omega^2 - \omega_a{}^2\right) + \left(\frac{\omega_g{}^2}{\omega^2} - 1\right) k_x{}^2 C_s{}^2 - k_z'{}^2 C_s{}^2 = 0. \qquad (2)$$

Here $\omega_a = \gamma g/2C_s$ is the acoustic cut-off frequency and $\omega_g = (\gamma - 1)^{1/2}g/C_s$ is the Brunt–Väisälä frequency. Typically $\omega_a/2\pi = 3.3$ mHz and $\omega_g/2\pi = 2.9$ mHz in the lower atmosphere. Propagating solutions, with $k_x$ and $k_z'$ real, exist for two frequency ranges: acoustic modes ($\omega > \omega_a$) are governed primarily by compression, whereas gravity modes ($\omega < \omega_g$) are governed primarily by buoyancy.

A non-isothermal, viscous atmosphere can be described in a similar way as long as linear and adiabatic approximations are still valid. The linearity of the problem allows for a spectral approach to describe the coupled seismic atmospheric wave propagation, as will be described in Section 4.

### 2.3 Coupling mechanism

Both acoustic and gravity waves can be launched by solid Earth events due to the continuity of vertical displacement and normal stress across the surface. Because of the imaginary part of $k_z$, the amplitudes of these waves grow as $\exp{(z/2H)}$ as they propagate upwards, allowing kinetic energy to be conserved while compensating for the exponential decrease in density. For a scaleheight of $H = 8$ km, an internal wave is amplified by a factor of $10^4$ at a height of 150 km. Therefore, even a small displacement (typically a fraction of millimetre) due to a Rayleigh wave can lead to vertical oscillations of several tens of metres at ionospheric height.

It should be noted that seismic waves as considered here are much more likely to produce strong atmospheric signals than many other natural or artificial sources, despite the very small size of the displacements they generate at the surface, as they present a unique combination of frequency and horizontal wavelength range necessary for an efficient coupling with acoustic modes of the atmosphere. These solid Earth events involve large amounts of energy. Although much smaller than the daily energy released by the solar radiation in the Earth's atmosphere, this energy is released in a frequency bandwidth, 0.005–0.1 Hz, where gravity waves and other sources

of atmospheric noise are quite low in amplitude. The small fraction of this energy transferred to the atmosphere leads, then, to a good signal-to-noise ratio. Other sources that could be considered present neither the frequency range nor the spatial coherence necessary for efficient coupling to the atmosphere (Fig. 2). In particular, in the short-wavelength limit, the acoustic cut-off frequency varies as $c/\lambda$, where $c$ is the sound speed and $\lambda$ the wavelength. Therefore, major energy from ocean swell, located in the same frequency range, may induce some infrasonic signal trapped at the base of the atmosphere (Garcés *et al.* 2003), but will not in general induce internal (i.e. upward propagating) acoustic waves in the atmosphere, because the wavelength is much shorter than for Rayleigh waves (Arendt & Fritts 2001).

## 3 OBSERVATIONS

### 3.1 Doppler ionospheric sounding

A high-frequency (HF) wave (3–30 MHz), emitted from the ground, is reflected by the ionosphere at the altitude where the local plasma frequency is equal to the signal frequency. With a wave emitted continuously at a given frequency, we can monitor the motion of the reflecting ionospheric layer through the Doppler frequency shift of sounding radio wave (Davies 1962). This technique is used in France by the Commissariat à l'Énergie Atomique (CEA). The CEA ionospheric network consists of one transmitter site at Francourville (FRC) and three receptor sites (Le Bardon LBD, Bois-Arnault BRN and Bruyères-le-Châtel BLC) 50–80 km away from Francourville (Fig. 3a). Ionospheric motion can be measured at two different altitudes using two sounding frequencies (3.849 and 4.624 MHz). The 3.849-MHz frequency is only used for the link FRC–BLC. More details about this network and recent results can be found in Farges *et al.* (2003).

### 3.2 Doppler sounding technique, noise level

The transmitted signal at FRC is a sinusoidal carrier of 3.849 or 4.624 MHz shifted by a few hertz. This frequency shift must be
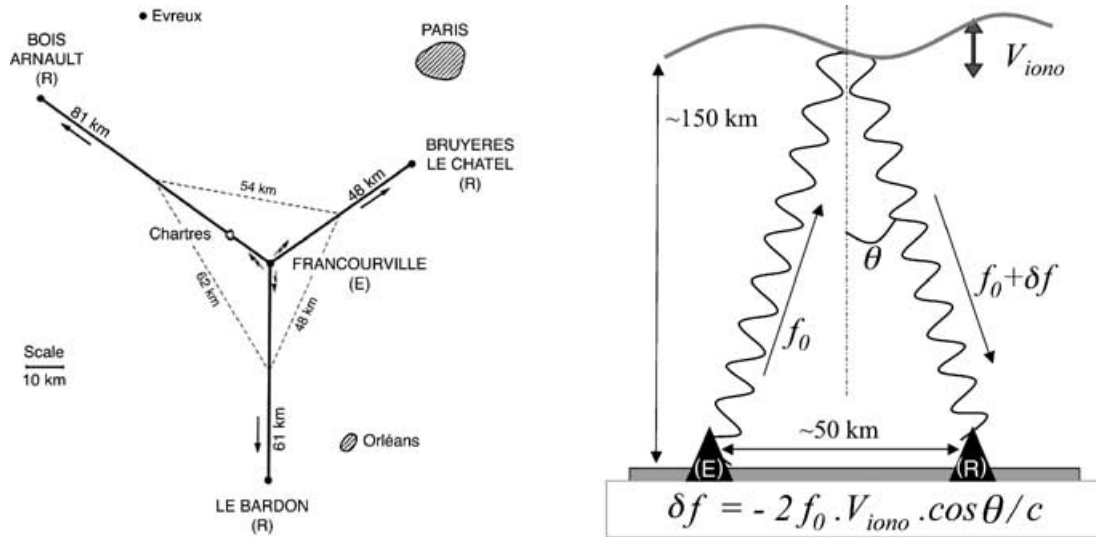
**Figure 3.** Doppler ionospheric sounding network of Francourville, France. On the right is the principle of measurement, on the left the geometry of the network: the measure of the Doppler shift in the radio signal between the transmitter (E) and the receiver (R) is directly related to the velocity of the reflecting ionospheric layer.

higher than the forecasted negative Doppler shift to avoid a spectral withdrawal. The receiver suppresses the carrier and digitizes the signal at the frequency of 50 samples per second. Spectra of the time-series are performed using a sliding Fast Fourier Transform (FFT) over a window of 82 s. The spectral resolution is then $1.2 \times 10^{-2}$ Hz. The slide of the FFT window is 0.64 s. For each spectrum, the frequency of the spectral peak, after deduction of the frequency shift brought to the transmitted signal, is taken as the Doppler shift for the time where the spectrum is calculated. These calculations give the temporal variation of the Doppler shift.

The relation between the vertical speed $v$ of the ionospheric layer and $\Delta f$, the measured Doppler shift, is

$$v = -\frac{\Delta f}{2F} \frac{c}{\cos \theta}, \tag{3}$$

where $F$ is the carrier frequency, $c$ the speed of light in a vacuum, and $\theta$ the angle of incidence of the sounding wave on the ionosphere (Fig. 3b). For the FRC sounding network, the ratio $1/\cos \theta$ is negligible and takes a value of between 1.005 and 1.01 for the FRC–BLC link. For a Doppler shift of 1 Hz, the absolute value of the vertical velocity of ionospheric motion is $39.3 \pm 0.5$ m s$^{-1}$ at 3.849 MHz and $32.7 \pm 0.4$ m s$^{-1}$ at 4.624 MHz. A negative (positive) Doppler shift means that the ionospheric layer reflecting the wave is rising (falling).

There is one main type of noise and one main error source. The main source of the noise is natural: there are a lot of acoustic and gravity waves propagating in the ionosphere. The waves that produce the largest Doppler shift perturbation are travelling ionospheric disturbances (TIDs). These TIDs are due to magnetic storms (Blanc & Mercandalli-Rascalou 1992) and atmospheric thunderstorms. They have a wave period of the order of 12 to 25 minutes. We can suppress the effects of these TIDs by filtering the temporal variation of the vertical velocity with a high-pass at 3.3 mHz (corresponding to periods of 5 minutes or lower).

The main source of error is technical. During nighttime, the efficiency of the Doppler sounding for the detection of Rayleigh-induced ionospheric waves is weaker than during daytime. Two facts may explain this. First, the HF radio emissions around the two carriers add noise over the signal to be digitized; moreover, the HF radio level is higher during the nighttime than during the daytime (a typical power ratio of 10), because of a lower attenuation of the HF wave during the night. Secondly, the reflecting altitude of the sounding wave is higher during the night than during the day, because of the lack of ionization source (principally the solar radiation); this implies a larger attenuation of the pressure wave at high frequencies during nighttime (a monochromatic wave is totally attenuated at 120 km height for a 1 s period, at 240 km height for a 10 s period).

### 3.3 Why does the Doppler sounding technique allow the measurement of seismic Rayleigh waves in the ionosphere?

Let us compare, for the situation following an earthquake, the ionospheric vertical motion with the ground-level vertical motion measured by a seismometer (Fig. 1). The comparison shows that, approximately 10 min after the Rayleigh wave arrival on the seismogram, a similar signal is measured in the ionosphere, in the same period range. This signal furthermore presents a similar dispersion to surface waves; its amplitude is, however, several order of magnitude higher than the ground motion recorded, and some of the short-period energy is missing.

The origin of this signal can be described as follows. Owing to the continuity of the vertical displacement and velocity, a seismic Rayleigh wave creates, at the ground–atmosphere boundary, a wave that has a velocity amplitude equal to the vertical motion of the ground (Le Pichon *et al.* 2002; Yuen *et al.* 1969). The pressure wave propagates near-vertically through the neutral atmosphere (Wolcott *et al.* 1984), with an incident angle $I$ less than 6° given by the Fresnel law and such that $\sin I = C_{\text{atmos}}/C_{\text{ground}}$. In the ionosphere, the neutral particles carry away the free electrons; thus the free electrons act like tracers of the neutral atmosphere perturbation. Their global vertical motion is measured by Doppler sounding.

Using data measured after the Costa Rica earthquake (Table 1), we confirm that the propagation from the earthquake takes place in the solid Earth principally as a Rayleigh wave, and then vertically from the surface to the ionospheric sounding point. The wave is detected first at the sounding point of the link FRC–BRN, which is the nearest to the epicentre (Fig. 4). The propagation velocity of the ionospheric perturbation is calculated with reference to the epicentre

**Table 1.** Earthquakes observed during this study. $(\delta z)_{max}$ is the peak-to-peak ground displacement observed at the ground, $(\delta f)_{max}$ is the peak-to-peak amplitude of the Doppler observation.

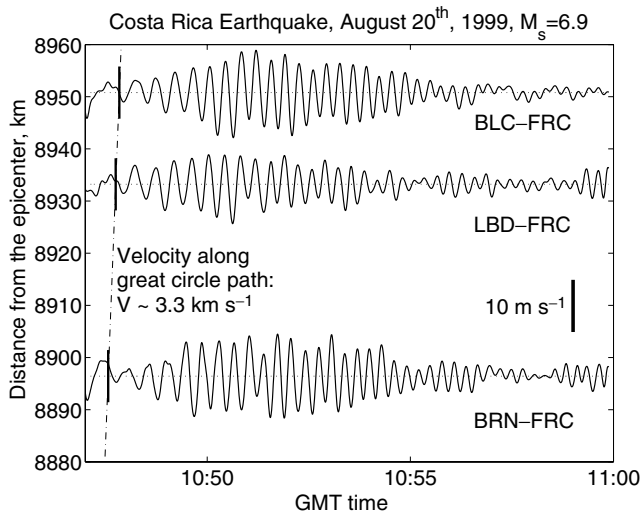| Date | Time (UT) | Location | Magnitude (USGS) | $(\delta z)_{max}$ (mm) | $(\delta f)_{max}$ (Hz) | Altitude (km) for 3.849 MHz | Altitude (km) for 4.624 Mhz |
|---|---|---|---|---|---|---|---|
| 08/17/99 | 00:01:39 | Turkey (Izmit) | $7.8 M_s$ | 5.5 | 0.5 | 235 | 240 |
| 08/20/99 | 10:02:21 | Costa Rica | $6.9 M_s$ | 0.3 | 0.4 | 150 | 170 |
| 09/20/99 | 17:47:18 | Taiwan (Chi-Chi) | $7.7 M_s$ | 1.6 | 0.3 | 168 | 186 |
| 09/30/99 | 16:31:15 | Oaxaca | $7.5 M_s$ | 1.0 | 0.15 | unknown | 170 |
| 10/16/99 | 09:46:44 | California | $7.4 M_s$ | 1.1 | 0.7 | 154 | 183 |
| 11/12/99 | 16:57:19 | Turkey | $7.5 M_s$ | 2.8 | 0.4 | 216 | 221 |
| 01/28/00 | 14:21:07 | Kuril Islands | $6.8 M_w$ | 0.4 | 0.15 | unknown | unknown |
| 03/28/00 | 11:00:22 | Bonin Island | $7.6 M_s$ | 1.8 | 0.8 | 137 | 162 |
| 05/04/00 | 04:21:16 | Sulawesi | $7.6 M_w$ | 0.3 | 0.3 | 226 | 280 |
| 06/04/00 | 16:28:25 | Southern Sumatera | $8.3 M_e$ | 1.0 | 0.4 | 142 | 168 |
| 06/18/00 | 14:44:13 | South Indian Ocean | $8.0 M_e$ | 3.4 | 1.1 | 143 | 169 |
| 11/16/00 | 07:42:16 | New Ireland | $7.8 M_s$ | 0.9 | 0.5 | 189 | N/A |



**Figure 4.** Ionospheric oscillations observed after the 1999 August 20 Costa Rica earthquake ($M_s = 6.9$) on the three different links. Time-series have been band-pass-filtered between 5 and 150 mHz. The apparent horizontal velocity of the perturbation along the great-circle path is approximately 3.3 km s$^{-1}$, which is consistent with a Rayleigh wave speed in this period range (20–35 s).

### 3.4 Data set

The main phase of observations considered in this paper is from 1999 August to 2000 December. During this period, 12 earthquakes were recorded (Table 1). We list in this Table all the earthquakes that give a clear response in the Doppler data. We indicate for each earthquake: the date and the time of the event; the magnitude determined by the USGS; the amplitude (peak-to-peak) of the vertical component of the seismic wave measured by the long-period seismograph of Lormes (France), located 270 km southeast of FRC; the amplitude of the Doppler shift measured for the FRC–BLC link; and the altitudes of reflection of the 3.849 and 4.624 MHz sounding waves.

These altitudes are determined by inversion of ionograms performed at Lannion (France) by France Telecom R& D (previously CNET). The ionosphere at these two sites (FRC and Lannion) can be

considered to be very similar because there are no other ionospheric perturbations during these 12 events. The ionogram sounding technique gives the vertical electron density profile of the ionosphere. This technique is not direct. Because the group velocity of the sounding wave is not equal to the speed of light in plasmas, an inversion program, such as POLAN (Titheridge 1985), must be used to determine the electron density profile. The vertical profile resolution is around 2–3 km.

## 4 MODELLING

### 4.1 Normal-mode summation

Normal-mode methods are commonly used in seismology to model seismic wave propagation in the whole Earth. This technique consists of calculating the discrete set of free oscillation modes of the solid Earth by solving the elastodynamic equation in the frequency domain. Summation of these modes allows us to model seismic wave propagation with a fairly good accuracy, either for a 1-D earth model or for 3-D earth models [for an extensive description of the theory see Dahlen & Tromp (1998) or (Lognonné & Clévédé 2002), the latter with software for the 1-D and 3-D cases].

Lognonné *et al.* (1998) extended normal-mode analysis to a spherical (1-D) earth model with a realistic atmosphere, i.e. with a neutral atmosphere layer added to the solid earth model, and taking into account a radiation boundary condition at the top of the model. This theory allows us to compute a complete set of normal modes including seismic, acoustic gravity and oceanic modes. Most modes have their energy localized either in the solid Earth, the ocean or in the atmosphere, but with a small amount transferred between the different parts of the model. The energy transferred from the seismic modes to the atmosphere varies from mode to mode, with a maximum found for frequencies that are related to fundamentals and harmonics of the atmospheric modes: for these modes, up to 0.04 per cent of the mode energy is found to reside in the atmosphere (Lognonné *et al.* 1998). Viscous dissipation in the atmosphere is the main attenuation factor for seismic acoustic waves and is included in this theory (Artru *et al.* 2001). Heat conductivity is less significant and is neglected in this study. Both the boundary condition and the viscosity induce a loss of energy in the system, and the normal modes obtained are complex functions of space, associated with complex frequencies. A summation technique for this type of mode has been developed previously for an anelastic and rotating earth model (Lognonné 1989, 1991; Tromp & Dahlen
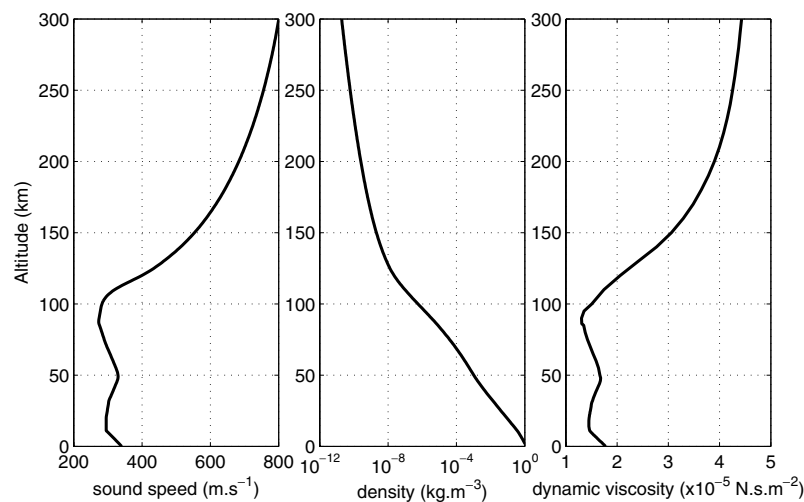
location and the earthquake time. In the period range 20–35 s, it is about 3.3 km s$^{-1}$, and therefore in the range of the Rayleigh wave speed (3–4 km s$^{-1}$).

**Figure 5.** Atmospheric model used for the simulations.

1990) and can be used straightforwardly in our case. The set of modes calculated (Fig. 2) can therefore be used to generate synthetic seismograms anywhere in the model from a given earthquake mechanism. In the following, we will use a catalogue composed of all 'solid' spheroidal fundamental and harmonic modes, for frequencies up to 50 mHz, to compute synthetic seismograms. The atmosphere model used (Fig. 5) was derived from NRLMSIS-00 (Picone *et al.* 2002) for mean atmospheric conditions at the location of the sounder. The viscosity profile was calculated from temperature and composition profiles following Banks & Kockarts (1973).

### 4.2 Validation

In order to validate the technique, we computed synthetics corresponding to the observed seismograms in France and Doppler records, using Harvard CMT for the source. The results of the simulation are presented in Figs 6 and 7. Fig. 6 shows broad-band signals (1–50 mHz) observed and calculated for the $M_w = 7.6$ Chi-Chi earthquake (Taiwan, 1999 September 20). The major differences found between data and normal-mode synthetics are present both for the ground and for the ionospheric signal. They are explained by the effect of the 3-D structure of the Earth, which is not included in the model. More accurate synthetics can indeed be obtained in the solid Earth using full 3-D simulations, as illustrated in the bottom panel of Fig. 6. In particular, lateral variations of the crustal structure are responsible for the large amount of 20-s period energy observed on both the data and the 3-D simulations.

At long periods, however, the quality of the normal-mode simulation is very good, as shown in Fig. 7 where the same data and synthetics have been low-pass-filtered to keep only periods longer than 100 s. The general waveforms are well recovered, although some discrepancies are still found in amplitudes and arrival time.

This demonstrates that solid Earth–atmosphere coupling is correctly taken into account in the adapted normal-mode approach. The limitations of our simulation in terms of waveform reconstruction are due to the 1-D nature of the solid earth model and could be corrected in the future by using a 3-D earth model and either spectral methods or higher-order perturbation theory methods (Lognonné & Clévédé 2002). In addition, the choice of the atmosphere model will influence predicted traveltimes and amplification of the perturbation in the atmosphere. For example, the daily variation of the

sound-speed profile would affect the arrival time of the acoustic ray at 200 km by 7–8 s.

## 5 COMPARISON AND FREQUENCY ANALYSIS

### 5.1 Data processing

The propagation of the seismic signal from the earthquake location to the ionosphere takes place mostly in the solid Earth, as a Rayleigh wave, and then almost vertically across the atmosphere in the Doppler sounding network vicinity. The signal is therefore mostly sensitive to lateral variations of the solid Earth structure, as we showed in the previous section. On the other hand, in the atmosphere the acoustic wave is sensitive only to the local atmospheric profile. The 1-D, normal-mode summation technique should therefore be able to predict correctly the atmospheric part of the propagation, provided that (1) the density, velocity and viscosity profiles used correspond to the local atmosphere, and (2) approximations made in the description of acoustic waves are valid. In order to validate our simulation, we compare the propagation properties of the signal predicted by our simulation with those deduced from the observations. The misfit already existing at ground level for periods shorter than 100 s prevents us from comparing the waveforms directly. However, as we consider a linear regime of acoustic wave propagation, the transfer function between the two altitudes of sounding should be the same for data and synthetics. We therefore chose to focus our analysis on the differential propagation time and amplification as a function of the frequency range.

We applied the same sequence of narrow band-pass filters to synthetics and observations, as shown in Fig. 8 for 168-km and 186-km data after the Chi-Chi earthquake. We compared these filtered time series from one altitude to another by cross-correlation and retrieved the time delay and amplitude ratio. We then performed the same procedure with the synthetics. Fig. 9 shows the result of this analysis performed on the synthetics and the data. The synthetics show a slight dispersion at long periods (i.e. propagation speed varies with frequency), as is expected from the acoustic gravity wave dispersion relation. The amplification decreases with frequency, corresponding to viscous attenuation. As for the Doppler data, despite some errors due to the sensitivity of the cross-correlation technique to noise level, the same processing produces similar trends: a
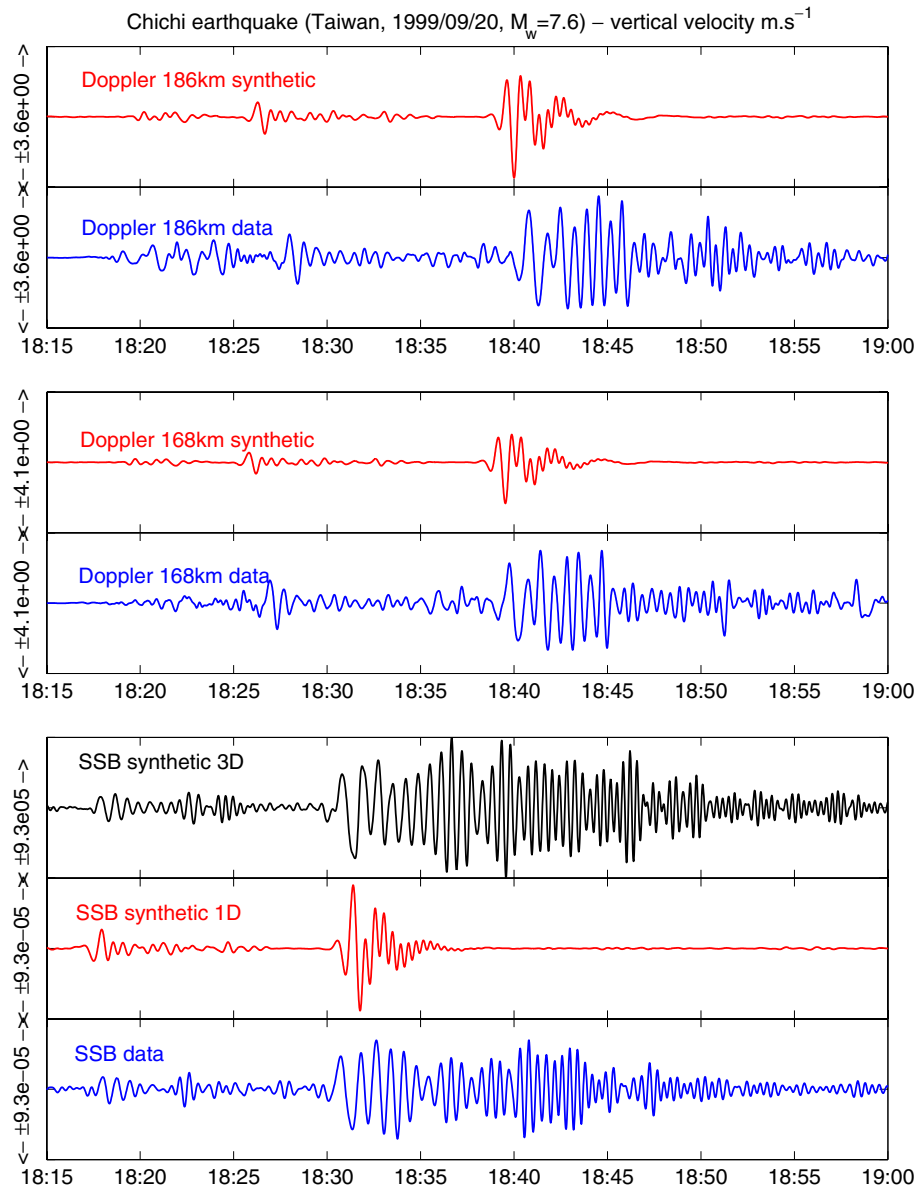
**Figure 6.** Rayleigh waves after the $M_w = 7.6$ Chi-Chi earthquake (Taiwan, 1999 September 20) as measured on a ground seismometer (bottom panel) at the Geoscope station SSB (Saint-Sauveur, France) and on the Francourville-to-Bruyères-le-Châtel link for the two Doppler sounding altitudes 168 and 186 km. Lower traces are data, top ones are normal-mode synthetics (top two panels). The top trace of the bottom panel is the result of a full 3-D simulation with a finite-source model (Ji *et al.* 2003), calculated by the spectral-element method (Komatitsch *et al.* 2002; Komatitsch & Tromp 2002a,b), courtesy of Chen Ji: it illustrates how the short-period discrepancies between 1-D synthetics and data are due to the 3-D structure of the solid Earth.

quasi-constant time delay (64 s for the data, 29 s for the synthetics), and an amplification factor that decreases as the frequency increases. The similarity is, however, limited to the overall aspect, and quantitatively we observe in the data significant discrepancies from what is predicted. First, the time delay between the two altitudes is much longer, with a more dispersive character at long periods. Secondly, the amplification is lower, showing in addition some low-frequency attenuation below 15 mHz.

### 5.2 Interpretation

Before looking into the details of these differences, we point out the effect of the relatively crude atmosphere model chosen for the simulation: as we used a constant 1-D model, it is possible that

the actual thermospheric temperature and density differ from those of the model, inducing some error in the sound velocity profile, possibly of up to 20 per cent.

The viscosity profile is also subject to large uncertainties. A quantitative interpretation of the overall amplitude and of the attenuation at short periods is therefore not possible at this stage. However, this uncertainty in the model is not sufficient to account for all the differences found, especially in terms of propagation velocity and low-frequency attenuation. Furthermore, error in the determination of the sounding altitudes (less than 3 km) cannot be responsible for more than 10 s of additional delay.

We performed the same data analysis for two other events: the California Hector Mine earthquake on 1999 October 16 (sounding altitudes 154 and 183 km) and the Indian Ocean earthquake on 2000
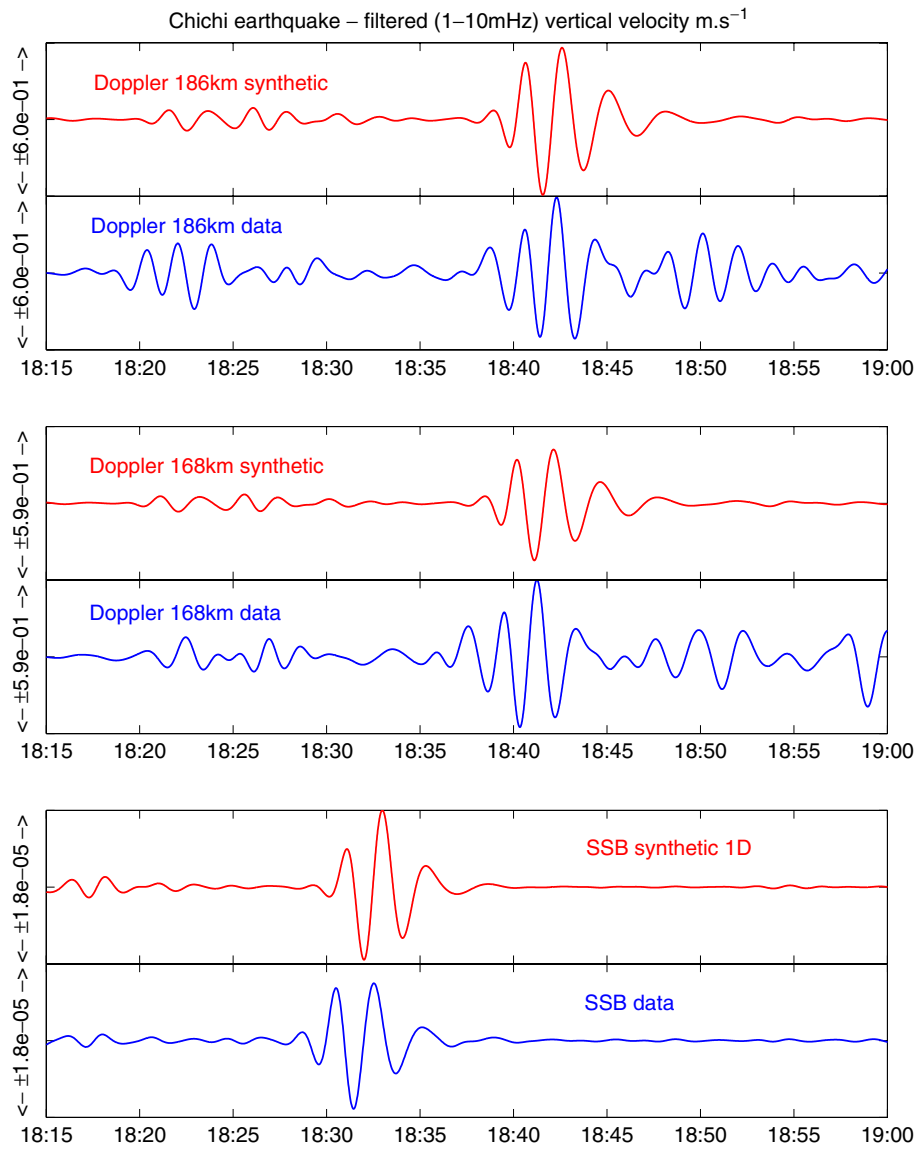
**Figure 7.** As Fig. 6, but after applying a band-pass filter between 1 and 100 mHz (100 to 1000 s). The 1-D simulation shows a fairly good agreement with observations in this period range.

June 18 (143 and 169 km). We summarize in Table 2 the time delays obtained and the inferred mean vertical velocities.

From the simulation we obtain, as expected, velocity estimates consistent with the sound velocity model, with an increase with altitude. On the other hand, data show a reasonable value for the ground to 168 km estimate, and then a decrease in velocity as the wave propagates upwards, down to 280 m s$^{-1}$ at 180 km. The latter velocity value is highly unlikely to correspond to the local sound speed.

This feature shows clearly that the formalism of acoustic gravity waves used in the simulation is not valid for the altitude range of the signals, as it would predict a wave travelling at the sound velocity. Let us review which effects are likely to appear as the wave propagates upwards.

*Horizontal winds* may affect the propagation of the acoustic wave (Calais & Minster 1995). In order to quantify the potential effect we estimated the deviation by ray tracing in the acoustic plane-wave limit in our 1-D atmosphere model completed by the Horizontal Wind Model (HWM) 1993 (Hedin *et al.* 1996). The wind model predicts, for 1999 September 20, at the location of the Doppler sounding network, a wind profile that ranges from −40 to 75 m s$^{-1}$ eastwards for the zonal wind, and from −30 to 5 m s$^{-1}$ northwards for the meridional wind. As the ray is nearly vertical, the only significant effect is a horizontal translation of the ray; however, the total deviation obtained from the ground up to 200 km is less than 10 km. The horizontal velocity of the perturbation is the Rayleigh wave velocity, and therefore this deviation affects the arrival time by less than 3 s.

*The thermal conduction* effect is similar to viscous attenuation, with a lesser or same-order influence on the wave propagation. It could be responsible for the low amplification factor observed.

*Non-linear propagation.* Advection terms are neglected throughout this simulation. The effect should, however, be small, as the perturbation in velocity is less than 5 per cent of the sound velocity. Qualitatively the effect is to transfer energy from lower to higher wavenumbers: this is probably the cause of the damping observed on the data at long periods.
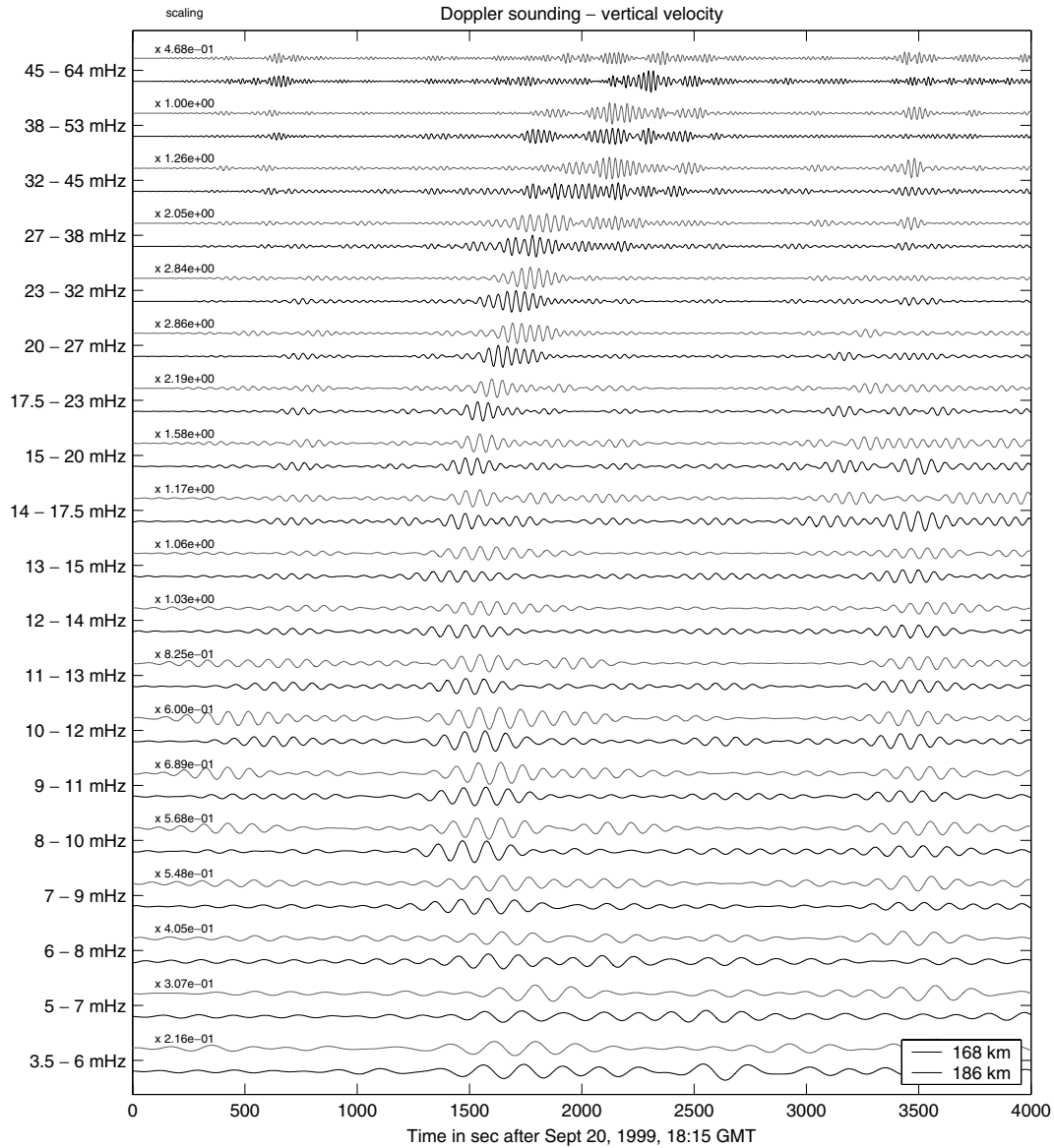
**Figure 8.** Doppler observation at two sounding frequencies corresponding to 168 km (black lines) and 186 km (grey lines) of altitude, after the Chi-Chi earthquake, filtered in several narrow frequency bands. The seismic signal consistently appears in those frequency bands, allowing for a frequency analysis of the propagation of the acoustic wave.

*Ionosphere dynamics.* As the wave reaches the ionospheric layers, the propagation should be described by the magnetohydrodynamics (MHD) formalism. The first effect involved is a damping of the wave due to ion drag (Yeh & Liu 1972), which appears at heights above 130 km. It is hard at this stage of our study to distinguish if the damping is due mainly to viscosity, thermal conduction or ion drag. Damping may also induce a slower wave propagation. It is, however, a second-order effect: we tested our simulation of the Chi-Chi earthquake with a viscosity five times larger in the upper atmosphere, and found a negligible (less than 1 s) increase in propagation time between the two sounding altitudes, whereas the attenuation of the wave was already stronger than in the data. Another interesting approach is perhaps to consider the simplified MHD equations in a magnetized plasma (Schunk & Nagy 2000): acoustic waves can no longer propagate perpendicularly to the magnetic field. In a very simple case (homogeneous plasma at high Alfvén speed), the dispersion relation for the slow magnetosonic wave reduces to $\omega/k =$

$C_s \cos\alpha$, where $C_s$ is the sound speed, and $\alpha$ is the angle between the wavevector $\mathbf{k}$ and the Earth's magnetic field. This effect could therefore account for the slow velocity observed at the altitude of the Doppler sounding, although a rough estimate in the case of the Chi-Chi earthquake gives only a 10 per cent decrease in velocity.

## 6 CONCLUSION

We have presented a study of infrasonic waves in the atmosphere induced by seismic waves. Ionospheric Doppler sounding allows the systematic detection and recording of such signals. Normal-mode theory adapted from seismology to include the atmosphere allows us to model the propagation of these waves from the earthquake sources up to the lower altitude of sounding. The synthetics obtained show a fairly good qualitative agreement with observation, with some limitations inherent to the 1-D modelling of seismic wave propagation, and others induced by the selected linear, adiabatic,
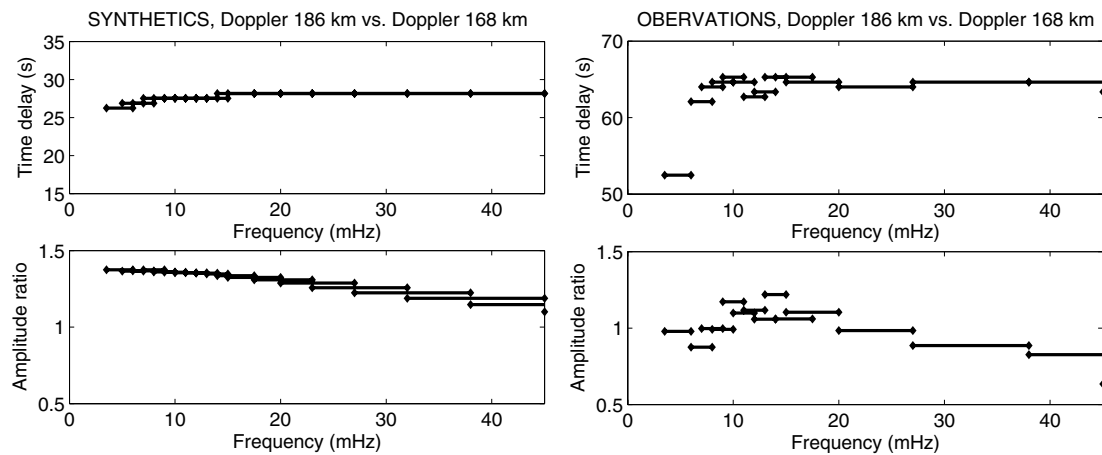
**Figure 9.** Differential arrival times and amplitudes for the Chi-Chi earthquake ionospheric signal. The left panel shows the results obtained from simulations, the right panel those from observations.

**Table 2.** Summary of the data analysis: * indicates that 13.5 s, corresponding to the ground propagation of the Rayleigh wave between SSB and FRC, was removed before estimating the mean velocity.

| Earthquake | Altitudes | Vertical distance | | Time delay | Mean velocity |
|---|---|---|---|---|---|
| Taiwan (Chi-Chi) | 168 and 186 km | 18 km | Data | 65 s | 280 m s$^{-1}$ |
| | | | *Synthetics* | *28 s* | *650 m s$^{-1}$* |
| California | 154 and 183 km | 29 km | Data | 88 s | 330 m s$^{-1}$ |
| | | | *Synthetics* | *45 s* | *640 m s$^{-1}$* |
| South Indian Ocean | 143 and 169 km | 26 km | Data | 57.5 s | 450 m s$^{-1}$ |
| | | | *Synthetics* | *45 s* | *577 m s$^{-1}$* |
| Taiwan (Chi-Chi) | Ground (SSB) and 168 km | 168 km (+50*) | Data | 422 s | 410* m s$^{-1}$ |
| | | | *Synthetics* | *434 s* | *399* m s$^{-1}$* |

neutral atmosphere formalism, which is inadequate to explain the ionospheric part of the propagation.

Comparison of the observed and calculated behaviour of the wave in the atmosphere can therefore provide quantitative information on acoustic propagation in the upper atmosphere, as the source of the perturbation is well constrained at ground level. Most differences between data and synthetics can be interpreted by considering the restrictive approximations implied in the modelling. Further study could allow a better understanding of the interaction of the atmospheric waves with the ionosphere.

## REFERENCES

Arendt, S. & Fritts, D.C., 2000. Acoustic radiation by ocean surface waves, *J. Fluid Mech.,* **415,** 1–21.

Artru, J., Lognonné, P. & Blanc, E., 2001. Normal modes modelling of postseismic ionospheric oscillations, *Geophys. Res. Lett.,* **28,** 697–700.

Banks, P.M. & Kockarts, G., 1973. *Aeronomy, part B,* Academic Press, New York.

Blanc, E., 1985. Observations in the upper atmosphere of infrasonic waves from natural or artificial sources: A summary, *Ann. Geophys.,* **3,** 673–688.

Blanc, E. & Mercandalli-Rascalou, B., 1992. Mid-latitude ionospheric disturbances produced by major magnetic storms, *Can. J. Phys.,* **70,** 553–565.

Bolt, B.A., 1964. Seismic air waves from the great alaska earthquake, *Nature,* **202,** 1095–1096.

Calais, E. & Minster, J.B., 1995. GPS detection of ionospheric perturbations following the January 17, 1994, Northridge earthquake, *Geophys. Res. Lett.,* **22,** 1045–1048.

Calais, E., Minster, J.B., Hofton, M.A. & Hedlin, M.A.H., 1998. Ionospheric signature of surface mine blasts from global positioning system measurements, *Geophys. J. Int.,* **132,** 191–202.

Dahlen, F.A. & Tromp, J., 1998. *Theoretical Global Seismology*, Princeton Univ. Press, Princeton.

Davies, K., 1962. The measurement of ionospheric drifts by means of a Doppler shift technique, *J. geophys. Res.,* **67,** 4909–4913.

Davies, K. & Baker, D., 1965. Ionospheric effects observed around the time of the Alaskan earthquake of March 28, 1964, *J. geophys. Res.,* **70,** 1251–1253.

Ducic, V., Artru, J. & Lognonné, P., 2003. Ionospheric remote sensing of the Denali earthquake Rayleigh surface waves, *Geophys. Res. Lett.,* **30,** 1951, doi:10.1029/2003GL017812.

Farges, T., Le Pichon, A., Blanc, E., Perez, S. & Alcoverro, B., 2003. Response of the lower atmosphere and the ionosphere to the eclipse of August 11, 1999, *J. atmos. terrest. Phys.,* **65**(6), 717–726.

Garcés, M., Hetzer, C., Merrifield, M., Willis, M. & Aucan, J., 2003. Ionospheric remote sensing of the observations of surf infrasound in Hawaii, *Geophys. Res. Lett.,* **30,** 2264, doi:10.1029/2003GL018614.

Hedin, A.E. *et al.*, 1996. Empirical wind model for the upper, middle, and lower atmosphere, *J. atmos. terrest. Phys.,* **58,** 1421–1447.

Hines, C.O., 1960. Internal atmospheric gravity waves, *Can. J. Phys.,* **38,** 1441–1481.

Ji, C., Helmberger, D.V., Wald, D.J. & Ma, K.-F., 2003. Slip history and dynamic implications of the 1999 chi-chi, Taiwan, earthquake, *J. geophys. Res.,* **108,** 2412, doi:10.1029/2002JB001764.

Komatitsch, D. & Tromp, J., 2002a. Spectral-element simulations of global seismic wave propagation—II. 3-D models, oceans, rotation, and gravity, *Geophys. J. Int.,* **150,** 303–318.

Komatitsch, D. & Tromp, J., 2002b. Spectral-element simulations of global seismic wave propagation—I. Validation, *Geophys. J. Int.,* **149,** 390–412.

Komatitsch, D., Ritsema, J. & Tromp, J., 2002. The spectral-element method, beowulf computing and global seismology, *Science,* **298,** 1737–1742.

Le Pichon, A., Guilbert, J., Vega, A., Garces, M. & Brachet, N., 2002. Ground-coupled air waves and diffracted infrasound from the arequipa earthquake of June 23, 2001, *Geophys. Res. Lett.,* **29,** 1886–1889.

Lognonné, P., 1989. Modélisation des modes propres de vibration dans une Terre anélastique et hétérogéne: Théorie et applications, *PhD thesis,* Université de Paris VII.

Lognonné, P., 1991. Normal modes and seismograms in an anelastic rotating earth, *J. geophys. Res.,* **96,** 20 309–20 319.

Lognonné, P. & Clévédé, E., eds, 2002. *Normal Modes of the Earth and Planets, Handbook on Earthquake and Engineering Seismology,* Vol. 81A, pp. 125–147, of Int. Geophys. Ser., Academic Press, London.

Lognonné, P., Clévédé, E. & Kanamori, H., 1998. Computation of seismograms and atmospheric oscillations by normal-mode summation for a spherical earth model with realistic atmosphere, *Geophys. J. Int.,* **135,** 388–406.

Picone, J.M., Hedin, A.E., Drob, D.P. & Aikin, A., 2002. Nrlmsise-00 empirical model of the atmosphere: Statistical comparisons and scientific issues, *J. geophys. Res.,* **107,** 1468, doi:10.1029/2002JA009430.

Schunk, R.W. & Nagy, A.F., 2000. *Ionospheres: Physics, Plasma Physics, and Chemistry*, Atmospheric and Space Science Series, Cambridge University Press, Cambridge.

Titheridge, J.E., 1985. Ionogram analysis with the generalized program POLAN, Word Data Center for Solar Terrestrial Physics, Tech. rep., UAG-93.

Tromp, J. & Dahlen, F.A., 1990. Free oscillations of a spherical anelastic earth, *Geophys. J. Int.,* **103,** 707–723.

Wolcott, J.H., Simons, D.J., Lee, D.D. & Nelson, R.A., 1984. Observation of an ionospheric perturbation arising from the coalinga earthquake of May 2, 1983, *J. geophys. Res.,* **89,** 6835–6839.

Yeh, K.C. & Liu, C.H., 1972. *Theory of Ionospheric Waves*, pp. 402–418, Academic Press, New York.

Yuen, P.C., Weaver, P.F., Suzuki, R.K. & Furumoto, A.S., 1969. Continuous travelling coupling between seismic waves and the ionosphere evident in May 1968 Japan earthquake data, *J. geophys. Res.,* **74,** 2256–2264.